

High spectral resolution test and calibration of an ultra-narrowband Faraday anomalous dispersion optical filter for use in daytime mesospheric resonance Doppler lidar

Jonathan S. Friedman^{a,*}, Darlene Maldonado-Nieves^a, Israel González^a, Jens Lautenbach^b, Xinzhao Chu^c, John A. Smith^c, Wentao Huang^c

^a NAIC Arecibo Observatory, Arecibo, Puerto Rico, USA

^b Leibniz Institute for Atmospheric Physics, Germany

^c University of Colorado, Boulder, CO, USA

ARTICLE INFO

Article history:

Received 4 August 2011

Received in revised form

23 January 2012

Accepted 25 January 2012

Available online 9 February 2012

Keywords:

Resonance Doppler lidar

Daytime lidar

Mesosphere

Faraday filter

ABSTRACT

We present a high-spectral-resolution test and calibration station for precision measurement of ultra-narrow bandwidth optical filters, and how this is used in the processing of daytime measurements from a resonance Doppler potassium lidar at Arecibo. The test station consists of Doppler-free saturation-absorption spectroscopy coupled with a small free-spectral-range Fabry–Perot etalon, which produces a precise measurement of the filter passband over a range of 20 GHz (40 pm) or more with a resolution of under 2 MHz. This setup is used to measure the bandpass function of a Faraday anomalous dispersion optical filter with a band center at 770 nm and full width at half maximum of about 3.64 GHz (~ 7.2 pm), which is the principal spectral filter in the Arecibo lidar. This bandpass function is then used to calibrate the Doppler-broadened returns from the K lidar. As the Faraday filter passband is narrow enough, the return lidar signals in both the resonance fluorescence and Rayleigh scattering are affected. We describe a calibration process to deconvolve the measured filter function from the return signals in order to achieve accurate temperature measurements. Our approach is demonstrated with actual lidar measurements.

© 2012 Elsevier Ltd. All rights reserved.

1. Introduction

Ultra-narrowband optical filters are becoming more and more commonly employed. They have applications in such diverse areas as communications and remote sensing. We employ ultra-narrowband filters for atmospheric lidar operations in daylight conditions. These filters are narrow enough that they affect the return signal by cutting off the spectral wings. For resonance Doppler lidar, this effect is on both the resonance signal, and, even more, on the Rayleigh scattering signal from the upper stratosphere that is used to calibrate the resonance signal.

Upper atmospheric lidars are the major means for regular monitoring of wind and temperatures in the upper mesosphere and lower thermosphere (MLT) between 80 and 105 km altitude. There are now a number of these lidars located in many parts of the world, but only a very few have the capability of making measurements in daylight. Nevertheless, daylight measurements

have shown to be a vital part of quantifying the energetics and dynamics of the MLT (States and Gardner, 1998, 2000a, 2000b; She, 2004; She et al., 2002, 2004; Chu et al., 2004; Plane et al., 2004; Fricke-Begemann and Höffner, 2005; Höffner and Lübken, 2007; Gardner et al., 2011). Understanding the effects of diurnal tides, gravity waves, and ion-neutral chemistry depend on making measurements day and night (Raizada et al., 2008; Tepley et al., 1981; She, 2004; She et al., 2004; States and Gardner, 2000a, 2000b; Fricke-Begemann and Höffner, 2005). We are therefore working to add daylight observing capabilities to more Doppler-resonance lidars. This work is being carried out in collaboration with the CEDAR (Coupling, Energetics, and Dynamics in Atmospheric Regions) Lidars Consortium Technology Center (CTC) (Chu et al., 2008), with the objectives of developing a standard, reliable filter design and disseminating technology and expertise to groups interested in daytime lidar observing.

The fact that the lidars use resonance lines in metal atoms presents the opportunity for deployment of a filter that depends on magneto-optical effects in a vapor composed of those very atoms. In a so-called magneto-optical filter (MOF), these effects are the means of dispersion, rather than interference, diffraction,

* Corresponding author. Tel.: +1 787 878 2612; fax: +1 787 878 1861.

E-mail address: jonathan@naic.edu (J.S. Friedman).

or refraction used in other narrowband filters. Two of the more mature lidar technologies measure sodium (the D_2 transition at 589 nm) and potassium (the D_1 transition at 770 nm). These metals turn out to have the property of high vapor pressure at relatively low temperature, which makes them practical for use in MOFs.

A Faraday Anomalous Dispersion Optical Filter (FADOF) is such a filter (Dick and Shay, 1991; Chen et al., 1993; Fricke-Begemann and Höffner, 2002; Höffner and Fricke-Begemann, 2005; Williams and Tomczyk, 1996). These have bandwidths of on the order of the Doppler broadening of the induced fluorescence of the mesospheric atoms being studied. The bandwidth is set based on a combination of vapor pressure of Na or K in an evacuated and heated cell and the axial magnetic field in which the vapor cell is placed. A combination of Faraday rotation, Zeeman effect, and optical dispersion, properly tuned, produces a high-throughput filter with a narrow transmission band, steep edges, and, for applications that require it, a wide acceptance angle. The filter is so narrow and its bandpass structure is such that it can affect the measurements, and this effect must be deconvolved from the recorded data in order to extract accurate Doppler information required for wind and temperature measurements.

In this paper, we describe the test station that we use to precisely determine the filter band structure for a K FADOF. We then describe how that calibration is used in the processing of the lidar data, in order to record temperatures in the upper atmosphere at any time of the day or night. We conclude with some initial results in the use of the FADOF for lidar measurements.

2. Faraday filter test station

2.1. Test station layout

The test station for the Arecibo Observatory potassium Doppler-resonance lidar layout is shown in Fig. 1. It is built around a single-longitudinal mode, tunable, external cavity diode laser (ECDL, EOSI model 2010). The laser can scan while maintaining single mode over a much broader bandwidth than that required to measure the filter passband. Its beam is split into four paths. One provides an absolute frequency marker with K saturation-absorption spectroscopy, the second provides a relative frequency marker with periodic steps over the full scan range using a Fabry–Perot etalon, the third goes to the filter we wish to measure, and the fourth monitors the laser power variations as it is tuned. The laser is tuned by a voltage scan provided from the analog output of the data acquisition system (DAQ), a National Instruments model USB-6229, and the four signals are recorded through analog inputs to the same DAQ.

The first sample split from the laser, at BS1, consists of two 4% reflections from a glass substrate. Another sample, split from BS1a, is overlapped with the second reflection from BS1 inside a cell containing K vapor (K cell) in a nearly counter-propagating configuration. In this way we record the saturated absorption spectrum of the K D_1 line, which is carried by the “probe” beam from BS1 to a photodiode (PD1) to record its intensity. The first reflection from BS1 is transmitted through the cell parallel to the beam from the second reflection and to an identical photodiode

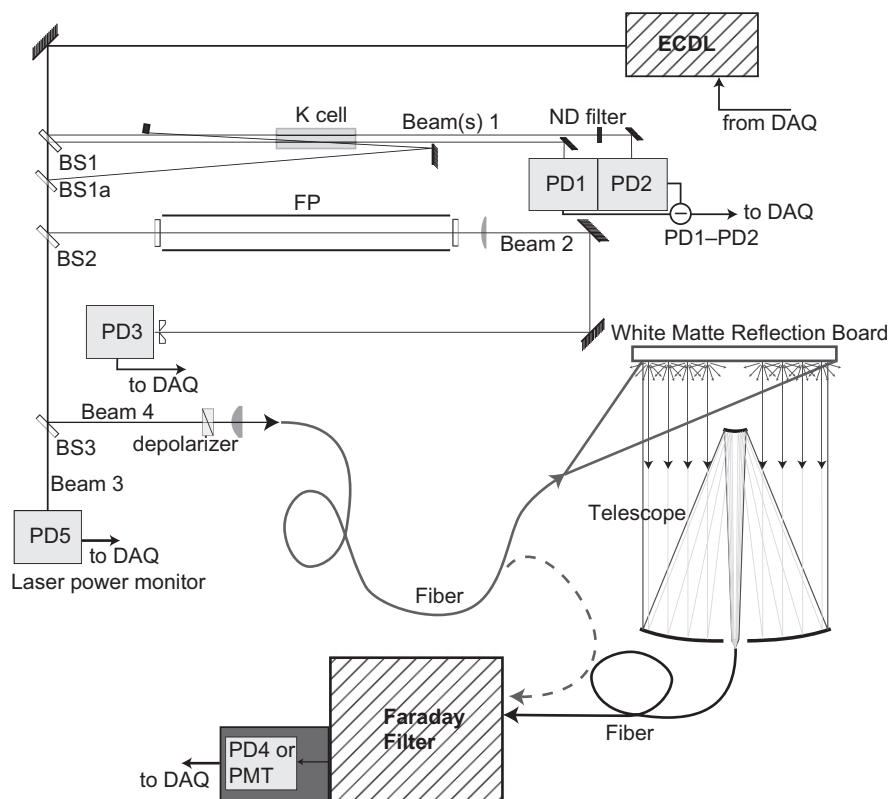


Fig. 1. Optical arrangement of the Faraday filter test station. The five separate beam paths are terminated by the detectors, PD1–PD5 (PD4 can be interchanged with a photomultiplier tube—PMT). PD1 and PD2 are for the Doppler-free spectroscopy, PD3 is for the Fabry–Perot etalon, PD4 or PMT is from the Faraday Filter (PD4 is used for the dashed fiber path to the filter, and PMT for the solid fiber path and telescope), and PD5 is the laser power monitor. These are sensed by analog inputs into a data acquisition system (the PMT through a photon counting system). The laser is controlled by the analog output of the data acquisition system. The beam can either be transmitted directly through the filter (dashed line) and detected by PD4, or it can be reflected from a white matte board placed at the mouth of the telescope, and the light that is concentrated on the receiver fiber is then transmitted through the filter and detected by a photomultiplier tube.

(PD2). It is used as a reference against PD1, as the signal in PD2 has only the direct absorption by the K vapor, while the signal in PD1 has both the direct and Doppler-free saturated absorption features. The signals are balanced both optically and electronically, and the result from PD2 is subtracted from that of PD1. The output of this differential measurement is a spectral scan with the direct Doppler-limited absorption cancelled out, and the residual signal is from the Doppler-free spectrum only. The spectrum is composed of 9 distinct and well-understood features that allow us to both establish an absolute spectral marker and to calibrate the Fabry–Perot etalon (FP). This process is explained in detail below in Section 3.1.

Beam two is transmitted through the FP, which consists of two flat mirrors separated by approximately 35 cm, and then into a third photodiode (PD3). This separation distance is not critical, however the large gap provides two important benefits. The first is to provide a large number of fringes over the range of the laser scan, which provides good precision in measuring the scan width, and the second is that it exposes nonlinearities in the scan to a high enough order that any important variations can be easily removed.

Beams 3 and 4 go to a power monitor and the FADOF, respectively. As with the K cell measurement, beam 3 acts a balance by which we can remove laser intensity variations that appear in the signal from beam 4. In this way, the ultimate signal is that of the FADOF transmission function alone. Beam 3 is directed into a fourth photodiode (PD4), while beam 4 follows one of two paths. For the measurements in this report, it is transmitted via a multimode optical fiber directly to the filter setup (dashed line), where it is launched through the filter and propagates to a Newport Model 818 calibrated photodiode detector with a model 1815-C power meter. For calibration of the filter for lidar measurements, we move this fiber (solid line) to where it can illuminate a matte white board that is placed atop the telescope. In this way, the light that propagates through the telescope is injected into the lidar receiver optical fiber, and thus to the Faraday filter, following the same path as the lidar return signal. This path provides some advantages for lidar operations.

Firstly, the beam characteristics within the filter are the same for both calibration and signal. Secondly, this light is detected by the receiver photomultiplier tube. Thirdly, we do not have to bother with switching a fiber in the heavily baffled receiver area, but only have to place the board atop the telescope. The zero level for the FADOF channel is established by blocking the laser on the test station bench. The FADOF has two-channels in order to collect light from both vertical and horizontal polarizations, and it was built with magnet-oven assemblies provided to the Arecibo Observatory by the Leibniz Institute for Atmospheric Physics (IAP) in Kühlungsborn, Germany and is described by Fricke-Begemann et al. (2002).

2.2. Control and acquisition software

We developed a system control and data acquisition software package in National Instruments' LabVIEW[®] for the test station. A screen shot is shown in Fig. 2. This software controls the scanning of the laser using a ramp signal fed to the piezo-electric that moves the cavity feedback-tuning mirror. The ramp is shown in the upper left graphic, labeled "Voltage out to Laser". The output is a linear ramp with roll-offs at the top and bottom in order to avoid high-frequency voltage variations that can damage the piezo. In the lower graph, labeled "Input Signal", the blue curve shows the FADOF signal. It is seen in both the slow forward scan and the faster return scan. The amplitude is in arbitrary units, so it does not represent an absolute filter transmission.

The other curves on the "Input Signal" plot are as follows. The white curve is from the Fabry–Perot etalon, showing a peak approximately every 430 MHz. The red curve is the signal from the Doppler-free hyperfine absorption spectrum of the D_1 line in potassium. The Doppler-free features are apparent in the center of the transmission peak for the filter, and they are shown in much greater detail in Fig. 3b, with seven of the nine peaks identified. In Fig. 2 there is a peak near the line center (the crossover feature) and dips on either side of the peak. Each of these peaks and dips is actually a triplet (Chu et al. 2008; Friedman et al., 2003; Hansch

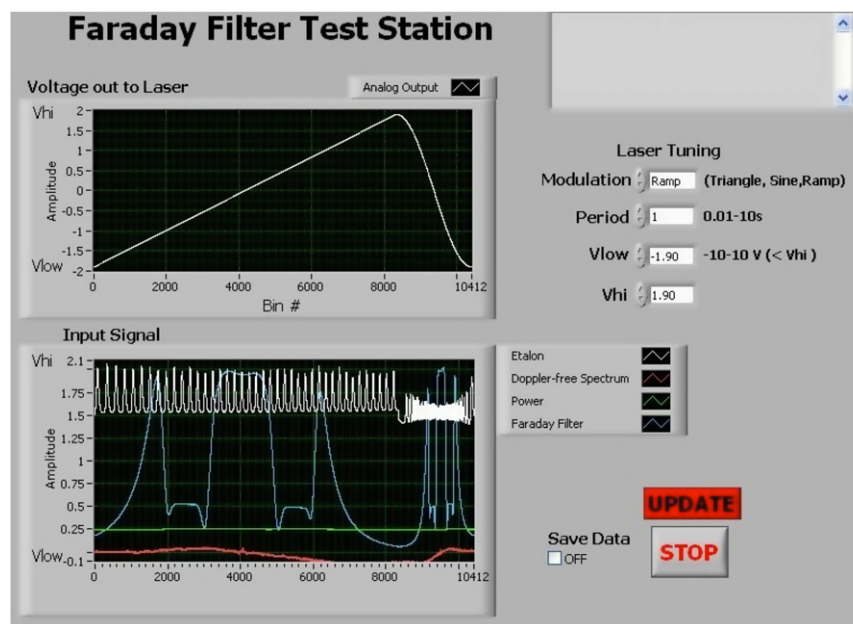


Fig. 2. Screen shot of the Faraday filter test station software. On the left-hand side, the upper window shows the voltage ramp used to tune the laser. The lower graphic shows: in white, the etalon scan, in red, the Doppler-free spectrum, in green, the laser power, and in blue, the filter function. On the right-hand side are controls, including ramp parameters (above) and start–stop and update buttons (below). The check box is to turn on and off data saving. (For interpretation of the references to color in this figure legend, the reader is referred to the web version of this article.)

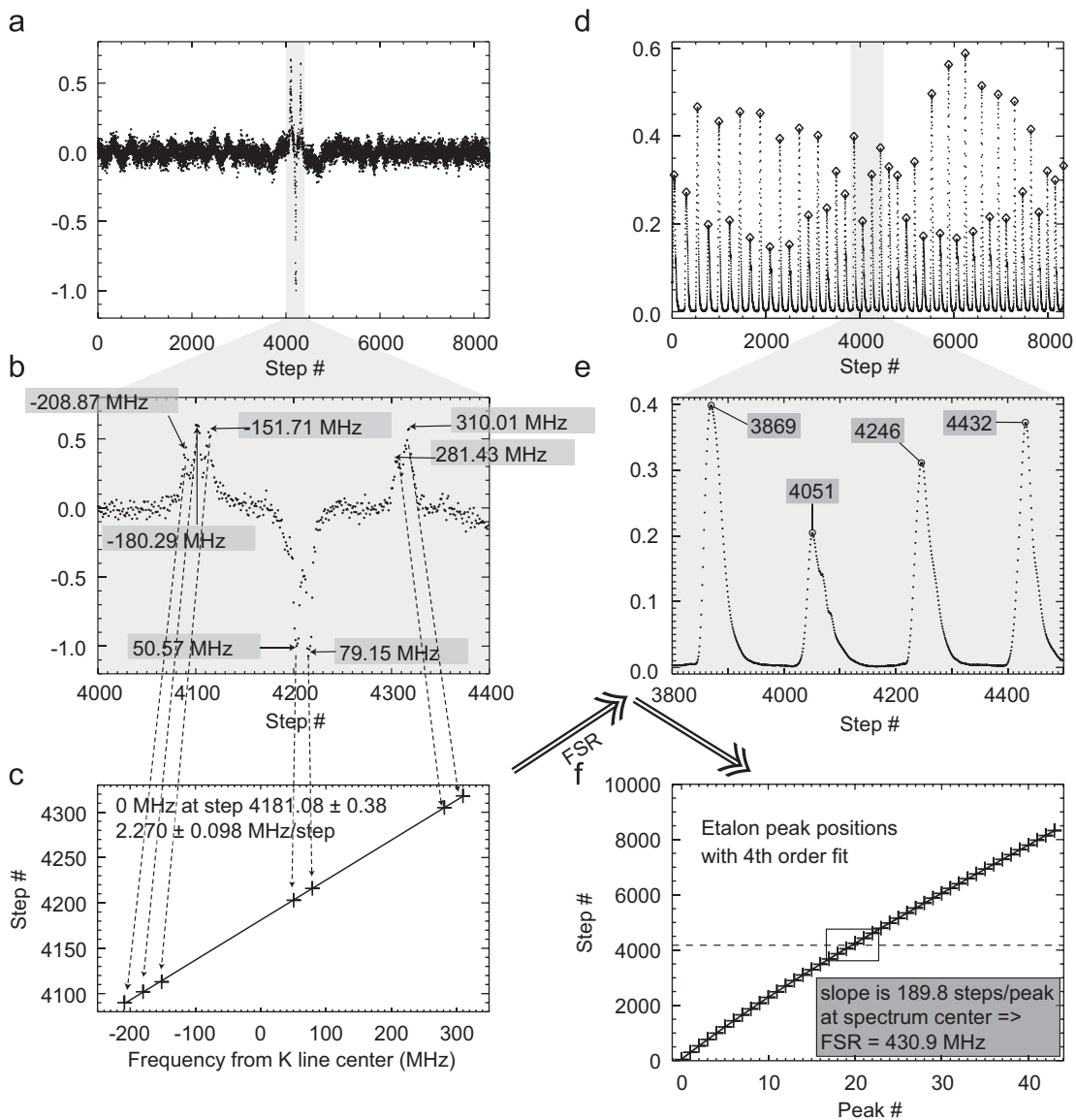


Fig. 3. Graphical description of the process of converting the Doppler-free spectrum and simultaneous etalon scan into a frequency scale. The shaded regions indicate magnification from the upper plot to the lower (a)–(b) and (d)–(e). On the left-hand side, the positions of the Doppler-free lines lead to a voltage-to-frequency scan step conversion and location of the spectral center. On the right-hand side, the fringe peak positions establish a frequency scale over the whole scan, calibrated to the etalon free spectral range, which is derived from the voltage-to-frequency factor.

et al., 1971), though the weaker peaks are obscured by noise in Figs. 2 and 3. Finally, the green curve is a measure of the laser power, which varies slightly over the scan.

3. Analysis

3.1. Filter bandpass function

The analysis of the test station data is described graphically in Fig. 3. Briefly, the processing steps are as follows:

1. Use the Doppler-free spectrum to calibrate the voltage scan steps to the frequency step size in the middle of the scan.
2. Use the Doppler-free spectrum to locate the spectrum center of mass based on the known spectral transitions.
3. Use the voltage-to-frequency calibration and the etalon fringe peaks in the same scan region to calculate the etalon free spectral range.

4. With the etalon peaks, create a frequency scale-versus-bin number, using a fourth-order polynomial fit. Align that frequency scale to the bin of zero frequency from step 1.
5. Remove the background levels from the signals in the FADOF and intensity channels, and then normalize the filter data to the laser power.

In detail, we use the positions of the Doppler-free spectrum features, shown in pane (a) and in detail in pane (b), to determine the frequency step of each voltage step from the DAQ. The step position versus frequency is fit to a line, from which, using the well-established absolute locations of the features, we determine the step size in MHz and the location of the center of mass of the K spectrum at 770.10929 nm (3.8928559×10^{14} Hz) (Banerjee et al., 2004). These are shown in Fig. 3c. Next, we use a peak finder to locate the fringe peaks from the etalon scan (pane d), and calculate the fractional voltage step positions of these peaks by fitting the peak positions to a 4th order polynomial and using the result to compensate for any nonlinearities in the laser scan

(Fig. 3f). The separations between the peaks in the vicinity of the Doppler-free features are used to determine the free spectral range of the etalon (Fig. 3c and e), which we have computed to be 430.9 MHz. Using the fit parameters for the scan, we can determine the relative frequency of each step throughout the spectrum. These are then scaled to the absolute spectrum as determined from the Doppler-free spectroscopy.

The accuracy and precision of the frequency scale come primarily from the voltage step size used to scan the measurement laser. This affects the determinations of the precise locations of the Doppler-free lines and of the etalon free spectral range (FSR), which are fundamental to the frequency scale of the bandpass spectrum. We use the Doppler-free spectrum in two ways to determine that scale. Firstly, it gives an absolute frequency reference for the spectrum. Secondly, the separation of the three sets of triplet lines gives precise locations in the laser scan, which are then used to calibrate the etalon FSR. The precisions of these calibrations are dependent on the voltage step size, the accuracy with which we can determine the fringe peak positions, and nonlinearities in the laser scan. All three can be determined from the data and analysis methods and are shown graphically in Fig. 3. The step size comes directly from the number of measurement data points per frequency as determined from the Doppler free spectrum, the accuracy of the fringe peak positions depends on the ability to precisely locate the peak positions to a fraction of a scan step, and the nonlinearity can be determined from the variation in spacing (in steps) between the etalon fringe peaks. The results of this analysis give a spectral resolution of ± 1.9 MHz.

Once we have the frequency scale, the filter bandpass function is normalized to the laser intensity, and we have a highly accurate measurement of the bandpass as a function of frequency. The result is shown in Fig. 4 by the solid line.

3.2. Filter effects on the data

In Fig. 4, along with the filter bandpass, we have plotted the resonance absorption spectrum from the K D₁ line at 200 K as a dashed line, and the emission lines from K D₁ excited by a laser tuned to -130 MHz from the spectral center are shown as vertical bars. The spectrum of Doppler-broadened Rayleigh scattering from the well-mixed atmosphere at 250 K is represented by color-coded dot-dashed lines based on the laser tuning, and assuming zero vertical wind at the measurement altitude of 40 km: the red curve is for the laser tuned to the red side of the spectrum, at -371 MHz,

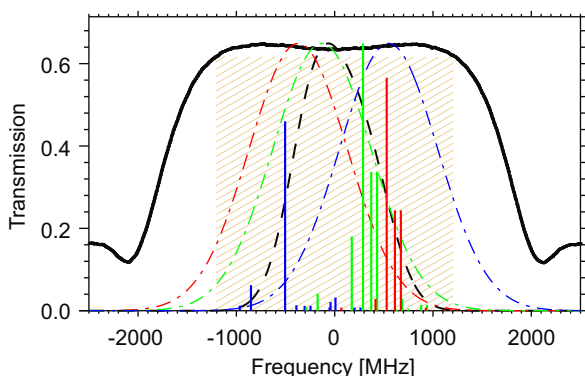


Fig. 4. Transmission spectrum of the Arecibo K Faraday filter (solid) is plotted with Rayleigh spectra from N₂ at 250 K at each of the three laser tunings (dash-dotted lines, red for -371 MHz, green for -130 MHz, blue for $+548$ MHz from the K spectral center), and the K D₁ resonance absorption spectrum at 200 K (dashed). The K D₁ emission lines are shown as vertical bars, red for laser frequency of -371 MHz, green for -130 MHz, and blue for $+548$ MHz. The shaded area represents the region of $>95\%$ of maximum transmission through the filter. (For interpretation of the references to color in this figure legend, the reader is referred to the web version of this article.)

the green curve is for -130 MHz, and the blue curve is for $+548$ MHz. The grayed-in central area shows the region of 95% of the maximum transmission through the filter. We detect emission from excited K atoms, which has a spectrum made up of individual lines, which are shown as the vertical bars in Fig. 4.

The full width at half maximum (FWHM) of the filter bandpass spectrum is about 3.64 GHz, while the 95% of maximum transmission region is 2.5 GHz wide. Fig. 4 shows that this filter has little impact on the resonance scatter, as all the emission lines lie within that region. Rayleigh scatter from the warmer stratosphere is more affected, with the wings falling outside of the 95% window. The emission spectra, which the lidar detects, are little affected by the filter. Note that, due to the velocity population of K atoms sampled by each laser tuning, emissions from atoms excited by the blue-shifted laser are seen red-shifted and vice-versa. There are 12 individual emission lines for each excitation, which are the result of 8 different absorption–emission paths and two degeneracies from each of two dominant isotopes, ³⁹K and ⁴¹K. For an explanation of the emission spectrum in Na, see Chen et al. (1996).

We use Rayleigh-scattered light from the stratosphere to calibrate the resonance scattering and compensate for variations in atmospheric transmission, so the Rayleigh signal affects both temperature and K density derivation. For this reason, the effect of the filter must be quantified. An accurate filter function is essential for this measurement. In Fig. 5 we show simulated temperature measurements with and without compensation for the filter. Panel (a) shows what the measurement looks like if we do not compensate (pluses) for the filter transmission for Rayleigh scatter versus when we do (squares). The compensated measurements assume a stratospheric temperature of 250 K at 40 km altitude. The middle plot shows that the error caused by neglecting the effect of the filter ranges from 12 K at 160 K to over 20 K at 240 K. We cannot directly measure the temperature of the stratosphere, so we are bound by this estimate and its associated uncertainty. In the bottom plot, we show the effect of that uncertainty, with the diamonds representing the temperature offset if the stratosphere is 10 K warmer than our estimate, and the pluses representing the temperature offset if the stratosphere is 10 K cooler than our estimate. These show that approximately 0.5–1 K offset is induced on the mesospheric temperatures for each 10 K error in the assumed stratospheric temperature.

The stability of the filter itself is critical to making accurate measurements. We maintain the temperature to within ± 0.1 °C of the set point. To determine the required stability, we generated a model to determine the uncertainty induced by vapor temperature variation. Fig. 6 shows the measured filter (black solid line) alongside three filter curves approximated by a model. We find that a magnetic field of 1700 Ga and vapor temperature of about 117 °C produces the closest fit to the filter (green dot-dashed line). (An idealized model cannot precisely fit the filter curve due to pressure broadening of the K D₁ spectrum, non-uniformities in the magnetic field, and differences between the two polarization channels.) We also plot filter curves for vapor temperatures 1 °C above and below the best fit temperatures, so the blue dashed line is for 116 °C and the red double-dot-dashed line is for 118 °C. The combined effect on the resonance and (primarily) the Rayleigh signal results in a clear effect on the temperatures derived from the data. Using the processing applied for Fig. 5, we find that a ± 1 °C change in the filter temperature results in a ± 5.5 K offset in the measured mesospheric temperature, so, by controlling the temperature within ± 0.1 °C, the error induced on the measurement is within ± 0.55 K. This demonstrates the importance of high thermal stability of the vapor cell ovens.

The lidar temperature computation algorithm is described by Friedman et al. (2003). This involves a ratio between the signal at wing frequencies and that for the center frequency. Stratospheric

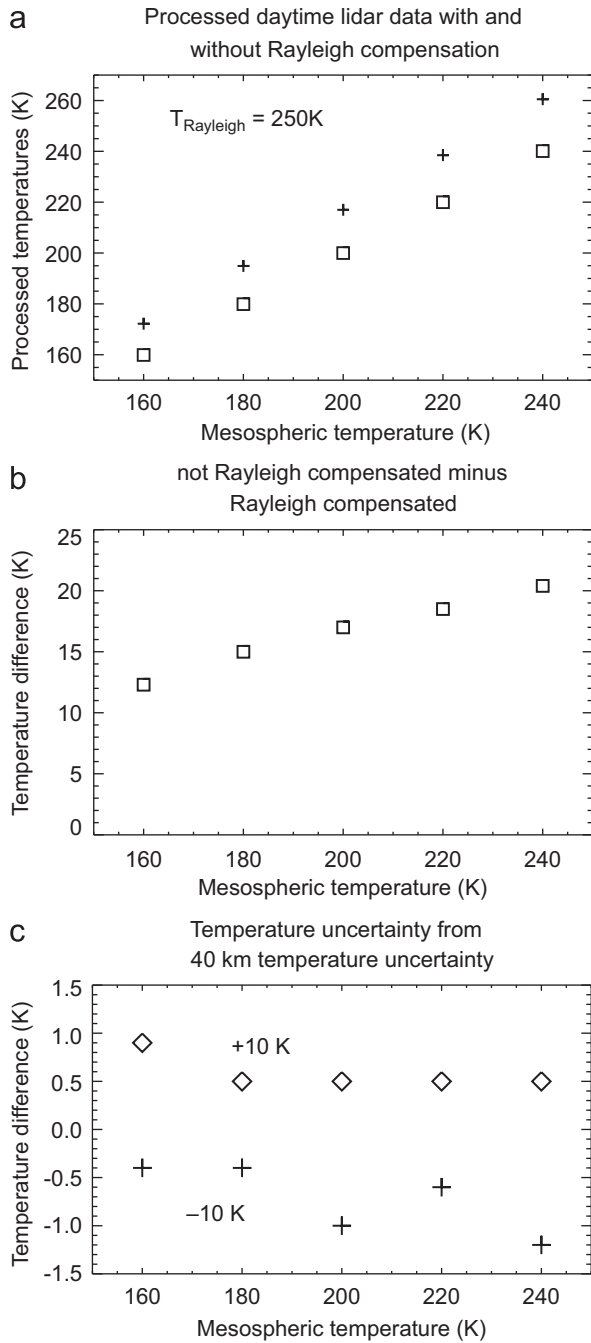


Fig. 5. The effect of compensation for the FADOF influence on Rayleigh-scattered light from the stratosphere, and its calibration of mesospheric temperatures. The upper plot (a) shows the compensated (squares) versus uncompensated (pluses) measurements. Plot (b) shows the difference between compensated and uncompensated. Plot (c) shows the effect of error in the assumed stratospheric temperature, with the diamonds for a stratospheric temperature 10 K warmer than, and the pluses 10 K cooler than the assumed temperature of 250 K. All are plotted as a function of the measured mesospheric temperature.

temperatures at 40 km to calibrate the K fluorescence signals come from MSIS-90 (Picone et al., 2002). Plotted in Fig. 7 is the temperature versus ratio with the filter out (solid line) versus with the filter in (dashed line). It is fortuitous that the lines cross between 180 and 200 K, which is precisely where temperatures in the 80–105 km region tend to fall at Arcibo's location. However, temperatures outside of this range do occur as shown in the climatology by Friedman and Chu (2007). Therefore, it is critical to perform accurate calibration for daytime measurements.

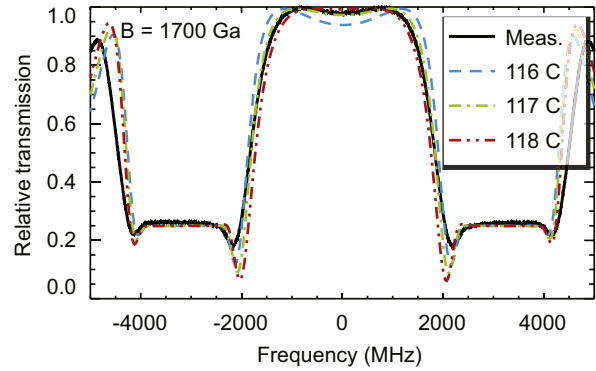


Fig. 6. The measured FADOF transmission is the black line. Modeled transmission functions are shown for $B=1700 \text{ Ga}$ and vapor temperatures of 116 °C (blue dashed), 117 °C (green dot-dashed), and 118 °C (red dot-dot-dashed). (For interpretation of the references to color in this figure legend, the reader is referred to the web version of this article.)

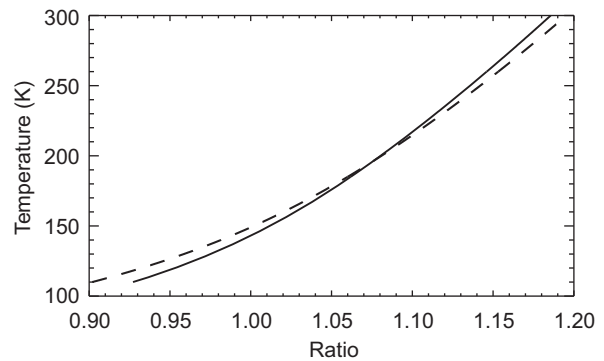


Fig. 7. Temperature versus temperature signal ratio for no-FADOF (nighttime) mode (solid line) and FADOF mode (dashed line).

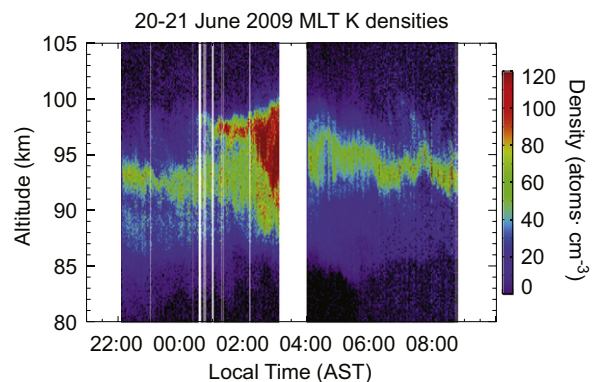


Fig. 8. K density observations from June 20 to 21, 2009 at Arcibo. The FADOF was in place for the post-04:00 data. Sunrise was at 05:53 AST (UT-4), and at 08:45, when operations ended, the solar elevation angle was 37°.

4. Lidar daytime measurements

First lidar measurements with the Faraday filter in place were made on February 5, 2009. Later, on June 20–21, 2009 we made our first Doppler measurements. Fig. 8 shows a plot of K density from observations that ran to 08:45 AST (12:45 UT). The solar elevation angle at that time was 37°. Measurements before 03:30 were made without the FADOF, which was installed for the post-04:00 measurements. The difference can be seen in the pre-dawn data, where the background noise with the filter in is considerably less

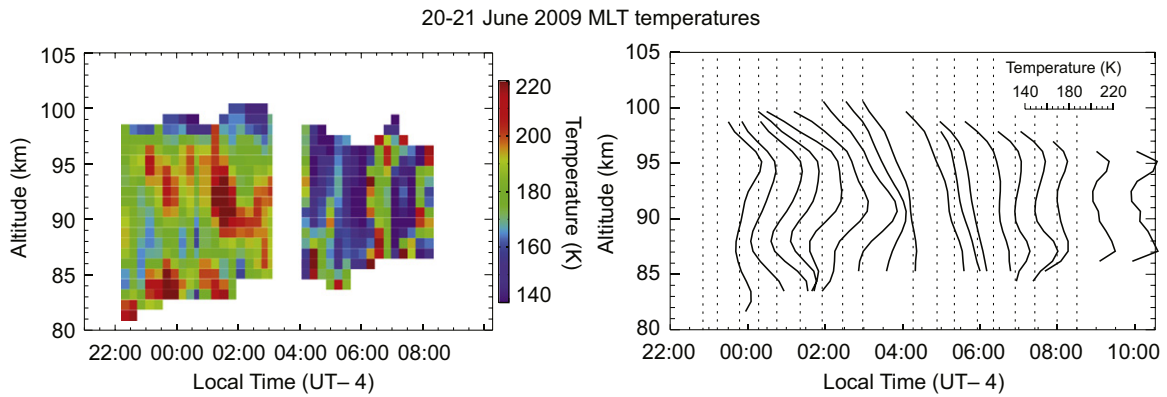


Fig. 9. Upper mesospheric temperature measurements from Arcicibo for June 20 to 21, 2009. On the left-hand side is a range-time-color plot with 15-min integrations and 0.9 km height bins. The data have been averaged with a 30 min, 1.8 km running mean. The FADOF was installed during the approximately 1 h gap between 3 and 4 AST. On the right-hand side, the same data are plotted with a stack plot, with 0.5 h and 0.9-km bins and smoothed with a 1 h \times 1.8 km running mean.

than without the filter (below about 84 km). After sunrise, at 05:53, the background can be seen to increase, though it asymptotes by around 08:00.

Fig. 9 shows temperature measurements from the same observations. We show the data in two formats. The first is a range-time-color depiction with 15-min and 0.9 km bins, with 0.5 h \times 1.8 km running mean smoothing. The second is a stack plot with 0.5 h \times 1.8 km averaging, and 1 h \times 1.8 km running mean smoothing. The time for each profile of the stack plot is indicated by the vertical dotted lines, which are also indicative of the minimum temperature – 140 K – for each profile. Sunrise was at 05:52 LT. These demonstrate effective operations with the FADOF under full daylight conditions to high solar elevation angles. Observations were terminated due to the arrival of clouds overhead.

Of particular interest for this paper in Fig. 9 is the extension of the warm temperature wave before and after 04:00 AST. Before 04:00 the lidar operated in “night mode”, with no FADOF, while after 4, we switched to the FADOF channel, yet the temperature structure appears to be consistent, indicating proper calibration of the lidar data. There are short-period (~ 2 h) waves that are strong throughout the altitude range after sunrise, and which are apparent at altitudes below 86 km during the night. In future observational studies we will look for repeated occurrences of such phenomena.

5. Discussion and conclusions

Regular operations of the Arcicibo potassium resonance Doppler lidar in daylight with a FADOF are still under development. Operating the filter presents an assortment of complications that must be overcome. The filter temperature must be stabilized to under 0.1 °C. This is achievable due to the small oven size and adequate thermal mass along with setting optimal feedback parameters for the temperature controller. Even with the filter, great care must be taken to baffle the receiver optics so as to eliminate any extraneous source of light entering the receiver. We also reduce the field of view to the minimum possible within the constraints of the limitations of the lidar instrument and the fluorescence process of the mesospheric K layer. We operate at a full angle divergence of 240 μ rad. Finally, sunlight striking the telescope structure causes it to heat, and the differential heating between the lit and shaded sides of the telescope disturbs the alignment. This has to be adjusted for in real time. Heating of the telescope also affects its focus and reduces the signal accordingly. These are the many factors that must be accounted for in order to have effective and reliable daylight operations with the lidar.

Ultra-narrow bandpass filters enable optical observations of the atmosphere by blocking the bright and broadband solar background. A Faraday Anomalous Dispersion Optical Filter (FADOF) is such a filter with ultra-high stability and Q-factor. As this filter is so narrow that it actually impacts the spectral observations, we have to measure precisely the filter bandpass function, and then deconvolve that from the data in order to obtain accurate measurements. In the case of the Arcicibo K Doppler-resonance lidar, those measurements are of upper mesospheric K densities and temperatures.

We have developed a system to make precise measurements of the filter bandpass function. This system consists of an external-cavity tunable diode laser, a Doppler-free absorption measurement system, a Fabry–Perot etalon, a laser power monitor, and a fiber to couple laser light to the filter. The laser provides a single-longitudinal mode source. The Doppler-free spectroscopy provides both an absolute frequency marker and a means to calibrate the etalon free spectral range. The etalon, in turn, provides a relative frequency marker, monitoring the laser scan and providing a means to compensate for its nonlinearities. The power monitor records a signal proportional to the laser power during the scan, so that this can be normalized out of the signal. The spectral precision is 1.9 MHz, and we see no reason that this cannot be considerably improved. However, given the relatively small effect of the filter on the measured mesospheric temperatures, this precision is far from a limiting factor in the lidar measurement precision.

Lidar measurements with the filter in place will greatly expand the science that can be undertaken. Given that Faraday filters are low-cost additions to lidar systems, it is of great interest that Doppler resonance lidars add them. Here, we have provided a recipe for users of FADOFs or other daylight filters for resonance lidar to precisely measure the filter function and using the results enhance the accuracy of the Doppler measurements.

Acknowledgments

The Arcicibo Observatory is operated by SRI International, in a consortium with Universities Space Research Association and Universidad Metropolitana, under a cooperative agreement with the National Science Foundation (AST-1100968). This work was supported at Arcicibo by NSF Grants ATM-0535457, ATM-0919786, and NSF-0630532. Lidar consortium technology center was supported by NSF Grant ATM-0545353. IG acknowledges support from the NASA-supported UPR-Mayagüez PaSSER program under Grant no. NNG04GD58G. DM was supported by the NAIC NSF-REU program. JSF sincerely thanks the Leibniz Institute for Atmospheric

Physics in Kühlungsborn, Germany, its director F.-J. Lübken, and Dr. J. Höffner, for the loan of the Faraday filter. The Faraday filter simulation was developed by S. Tomczyk, and modified by B.P. Williams and J. Hedin.

References

- Banerjee, A., Das, D., Natarajan, V., 2004. Precise measurements of atomic energy levels: *D* lines and fine-structure interval in K. *Journal of the Optical Society of America B* 21 (1), 79–82. doi:10.1364/JOSAB.21.000079.
- Chen, H., She, C.Y., Searcy, P., Korevaar, E., 1993. Sodium-vapor dispersive Faraday filter. *Optics Letters* 18, 1019–1021.
- Chen, H., White, M.A., Krueger, D.A., She, C.Y., 1996. Daytime mesopause temperature measurements with a sodium-vapor dispersive Faraday filter in a lidar receiver. *Optics Letters* 21 (15), 1093–1095.
- Chu, X., Nott, G.J., Espy, P.J., Gardner, C.S., Dietrich, J.C., Clilverd, M.A., Jarvis, M.J., 2004. Lidar observations of polar mesospheric clouds at Rothera, Antarctica (67.5°S, 68.0°W). *Geophysical Research Letters* 31, L02114. doi:10.1029/2003GL018638.
- Chu, X., Huang, W., Friedman, J.S., Brown, A.T., 2008. CRRL/CTC: Doppler-free saturation-absorption and polarization spectroscopy for resonance fluorescence doppler lidars. In: *Proceedings of the 24th International Laser Radar Conference, Organizing Committee of the 24th International Laser Radar Conference*, pp. 809–812.
- Fricke-Begemann, C., Alpers, M., Höffner, J., 2002. Daylight rejection with a new receiver for potassium resonance temperature lidars. *Optics Letters* 27, 1932–1934.
- Fricke-Begemann, C., Höffner, J., 2005. Temperature tides and waves near the mesopause from lidar observations at two latitudes. *Journal of Geophysical Research* 110 (D9), 19,103. doi:10.1029/2005JD005770.
- Friedman, J.S., Tepley, C.A., Raizada, S., Zhou, Q.H., Hedin, J., Delgado, R., 2003. Potassium Doppler-resonance lidar for the study of the mesosphere and lower thermosphere at the Arecibo Observatory. *Journal of Atmospheric and Solar-Terrestrial Physics* 65 (16–18), 1411–1424. doi:10.1016/S1364-6826(03)00205-0.
- Gardner, C.S., Chu, X., Espy, P.J., Plane, J.M.C., Marsh, D.R., Janches, D., 2011. Seasonal variations of mesospheric Fe layers at Rothera, Antarctica (67.5°S, 68.0°W). *Journal of Geophysical Research* 116, D02304. doi:10.1029/2010JD014655.
- Hänsch, T.W., Shahin, I.S., Schawlow, A.L., 1971. High resolution saturation spectroscopy of the sodium *D* lines with a pulsed tunable dye laser. *Physical Review Letters* 27 (11), 707–710. doi:10.1103/PhysRevLett.27.707.
- Höffner, J., Fricke-Begemann, C., 2005. Accurate lidar temperatures with narrow-band filters. *Optics Letters* 30 (8), 890–892. doi:10.1364/OL.30.000890.
- Höffner, J., Lübken, F.-J., 2007. Potassium lidar temperatures and densities in the mesopause region at Spitsbergen (78°N). *Journal of Geophysical Research* 112, D20114. doi:10.1029/2007JD008612.
- Picone, J.M., Hedin, A.E., Drob, D.P., Aikin, A.C., 2002. NRLMSISE-00 empirical model of the atmosphere: statistical comparisons and scientific issues. *Journal of Geophysical Research* 107 (A12), 1468. doi:10.1029/2002JA009430.
- Plane, J.M.C., Murray, B.J., Chu, X., Gardner, C.S., 2004. Removal of meteoric iron on polar mesospheric clouds. *Science* 304, 426–428.
- States, R.J., Gardner, C.S., 1998. Influence of the diurnal tide and thermospheric heat sources on the formation of mesospheric temperature inversion layers. *Geophysical Research Letters* 25, 1483–1486.
- She, C.Y., Chen, S., Williams, B.P., Hu, Z., Krueger, D.A., 2002. Tides in the mesopause region over Fort Collins, Colorado (41°N, 105°W) based on lidar temperature observations covering full diurnal cycles. *Journal of Geophysical Research* 107 (D18), 4350. doi:10.1029/2001JD001189.
- She, C.Y., 2004. Initial full-diurnal-cycle mesopause region lidar observations: diurnal-means and tidal perturbations of temperature and winds over Fort Collins, CO (41°N, 105°W). *Journal of Atmospheric and Solar-Terrestrial Physics* 66, 663–674. doi:10.1016/j.jastp.2004.01.037.
- She, C.Y., Li, T., Collins, R.L., Yuan, T., Williams, B.P., Kawahara, T.D., Vance, J.D., Acott, P.E., Krueger, D.A., 2004. Tidal perturbations and variability in the mesopause region over Fort Collins, CO (40°N, 105°W): continuous multi-day temperature and wind lidar observations. *Geophysical Research Letters* 31, L24,111. doi:10.1029/2004GL021165.
- States, R.J., Gardner, C.S., 2000a. Thermal structure of the mesopause region (80–105 km) at 40°N latitude. Part I: seasonal variations. *Journal of the Atmospheric Sciences* 57 (1), 66–77.
- States, R.J., Gardner, C.S., 2000b. Thermal structure of the mesopause region (80–105 km) at 40°N latitude. Part II: diurnal variations. *Journal of the Atmospheric Sciences* () 57 (1), 78–92.
- Williams, B.P., Tomczyk, S., 1996. Magneto-optic Doppler analyzer: a new instrument to measure mesopause winds. *Applied Optics* 35 (33), 6494–6502.